



HAL
open science

Lychee-like TiO₂@Fe₂O₃ Core-Shell Nanostructures with Improved Lithium Storage Properties as Anode Materials for Lithium-Ion Batteries

Yuan Chen, Feihong Liu, Yufei Zhao, Mengdie Ding, Juan Wang, Xuan Zheng, Huihu Wang, Marie-Christine Record, Pascal Boulet

► To cite this version:

Yuan Chen, Feihong Liu, Yufei Zhao, Mengdie Ding, Juan Wang, et al.. Lychee-like TiO₂@Fe₂O₃ Core-Shell Nanostructures with Improved Lithium Storage Properties as Anode Materials for Lithium-Ion Batteries. *Materials*, 2023, 16 (5), pp.1945. 10.3390/ma16051945 . hal-04046591

HAL Id: hal-04046591

<https://amu.hal.science/hal-04046591>

Submitted on 26 Mar 2023

HAL is a multi-disciplinary open access archive for the deposit and dissemination of scientific research documents, whether they are published or not. The documents may come from teaching and research institutions in France or abroad, or from public or private research centers.

L'archive ouverte pluridisciplinaire **HAL**, est destinée au dépôt et à la diffusion de documents scientifiques de niveau recherche, publiés ou non, émanant des établissements d'enseignement et de recherche français ou étrangers, des laboratoires publics ou privés.



Distributed under a Creative Commons Attribution 4.0 International License

Article

Lychee-like $\text{TiO}_2@Fe_2O_3$ Core-Shell Nanostructures with Improved Lithium Storage Properties as Anode Materials for Lithium-Ion Batteries

Yuan Chen ^{1,2,3} , Feihong Liu ¹, Yufei Zhao ¹, Mengdie Ding ¹, Juan Wang ^{1,2,3,*}, Xuan Zheng ^{1,2,3}, Huihu Wang ^{1,2,3}, Marie-Christine Record ^{2,4,*}  and Pascal Boulet ^{2,5} 

- ¹ Hubei Provincial Key Laboratory of Green Materials for Light Industry, Collaborative Innovation Center of Green Light-Weight Materials and Processing, and School of Materials and Chemical Engineering, Hubei University of Technology, Wuhan 430068, China
- ² New Materials and Green Manufacturing Talent Introduction and Innovation Demonstration Base, Wuhan 430068, China
- ³ Hubei Longzhong Laboratory, Xiangyang 441000, China
- ⁴ Aix-Marseille University, Faculty of Sciences, IM2NP, CEDEX 20, 13397 Marseille, France
- ⁵ Aix-Marseille University, Faculty of Sciences, Madirel, CEDEX 20, 13397 Marseille, France
- * Correspondence: jwang@hbut.edu.cn (J.W.); m-c.record@univ-amu.fr (M.-C.R.)

Abstract: In this study, lychee-like $\text{TiO}_2@Fe_2O_3$ microspheres with a core-shell structure have been prepared by coating Fe_2O_3 on the surface of TiO_2 mesoporous microspheres using the homogeneous precipitation method. The structural and micromorphological characterization of $\text{TiO}_2@Fe_2O_3$ microspheres has been carried out using XRD, FE-SEM, and Raman, and the results show that hematite Fe_2O_3 particles (7.05% of the total mass) are uniformly coated on the surface of anatase TiO_2 microspheres, and the specific surface area of this material is $14.72 \text{ m}^2 \text{ g}^{-1}$. The electrochemical performance test results show that after 200 cycles at 0.2 C current density, the specific capacity of $\text{TiO}_2@Fe_2O_3$ anode material increases by 219.3% compared with anatase TiO_2 , reaching 591.5 mAh g^{-1} ; after 500 cycles at 2 C current density, the discharge specific capacity of $\text{TiO}_2@Fe_2O_3$ reaches 273.1 mAh g^{-1} , and its discharge specific capacity, cycle stability, and multiplicity performance are superior to those of commercial graphite. In comparison with anatase TiO_2 and hematite Fe_2O_3 , $\text{TiO}_2@Fe_2O_3$ has higher conductivity and lithium-ion diffusion rate, thereby enhancing its rate performance. The electron density of states (DOS) of $\text{TiO}_2@Fe_2O_3$ shows its metallic nature by DFT calculations, revealing the essential reason for the high electronic conductivity of $\text{TiO}_2@Fe_2O_3$. This study presents a novel strategy for identifying suitable anode materials for commercial lithium-ion batteries.

Keywords: lithium-ion batteries; anode materials; $\text{TiO}_2@Fe_2O_3$ microspheres; electrochemical properties; first-principles calculations



Citation: Chen, Y.; Liu, F.; Zhao, Y.; Ding, M.; Wang, J.; Zheng, X.; Wang, H.; Record, M.-C.; Boulet, P. Lychee-like $\text{TiO}_2@Fe_2O_3$ Core-Shell Nanostructures with Improved Lithium Storage Properties as Anode Materials for Lithium-Ion Batteries. *Materials* **2023**, *16*, 1945. <https://doi.org/10.3390/ma16051945>

Academic Editor: Alessandro Dell'Era

Received: 4 February 2023

Revised: 21 February 2023

Accepted: 24 February 2023

Published: 27 February 2023



Copyright: © 2023 by the authors. Licensee MDPI, Basel, Switzerland. This article is an open access article distributed under the terms and conditions of the Creative Commons Attribution (CC BY) license (<https://creativecommons.org/licenses/by/4.0/>).

1. Introduction

With the increase in energy consumption and environmental issues, lithium-ion batteries have attracted considerable interest as a form of energy storage technology [1–3]. Due to its low specific capacity and poor cycle performance at high current densities, it is increasingly challenging for commercial graphite to match the needs of lithium-ion batteries [4,5]. As a result, new commercial anode materials are required [6]. Due to their theoretical capacity, high power density, and abundance of resources, transition metal oxides have become a research hotspot for lithium-ion battery anode materials [7]. Nevertheless, the majority of transition metal oxides (including Fe_2O_3 [8], Fe_3O_4 [9], MnO_2 [10], Mn_2O_3 [11], Mn_3O_4 [12], MnO [13], CuO [14], NiO [15], and Co_3O_4 [16]) used as anode materials for lithium-ion batteries typically experience significant volume expansion effects during the lithium insertion/extraction process. As an anode material for lithium-ion batteries, TiO_2 possesses high insertion/extraction lithium-ion potential and a stable insertion/extraction

lithium-ion structure in addition to high coulombic efficiency, cheap cost, stable chemical characteristics, and environmental friendliness [17,18]. However, the low electronic conductivity of TiO₂ anode materials, as well as the low diffusion coefficient of lithium-ion within them, is insufficient for commercial applications.

Currently, TiO₂ anode material optimization measures are primarily focused on two aspects: nanosizing and material compounding [4]. The nanoscale TiO₂ anode materials can increase the contact area between the anode materials and the electrolyte, reduce the lithium-ion transport channel within the materials, and provide additional lithium-ion storage sites. Yao et al. [19] manufactured hollow spherical TiO₂ anode materials, Zhao et al. [20] constructed interconnected TiO₂ nanofiber anode materials, and Lu et al. [21] produced nanowire TiO₂ anode materials. Compounding TiO₂ with other materials can also effectively enhance the performance of anode materials [22–25]. Guan et al. [26] coated TiO₂ with TiOF₂, Wang et al. [27] covered a layer of MgCo₂O₄ on the surface of TiO₂, and Li et al. [28] compounded TiO₂ with C/FeS₂.

Fe₂O₃, as a transition metal oxide, has the advantages of low cost, high theoretical capacity, abundant resources, and low power density, and therefore has attracted the interest of researchers [29,30]. The literature indicates that Fe₂O₃ and TiO₂, two anode materials, have a synergistic effect [30,31], i.e., the composite of structurally stable TiO₂ and Fe₂O₃ with a high theoretical capacity can effectively raise the specific capacity of the anode materials. In addition, these materials are inexpensive, abundant in resources, environmentally friendly and pollution-free, and appropriate for large-scale applications. The majority of current studies on the composite of these two materials concentrate on using Fe₂O₃ as a substrate and utilizing TiO₂ as a stable coating layer to address the problem of high-volume expansion of Fe₂O₃ [4,25,31]. However, less research has been conducted on the issue of the poor specific capacity of TiO₂ when combined with Fe₂O₃ on a TiO₂ substrate.

In this study, the lychee-like core-shell structure TiO₂@Fe₂O₃ microspheres were prepared by coating a layer of Fe₂O₃ particles on the surface of homemade TiO₂ mesoporous microspheres using the homogeneous precipitation method. In order to investigate the connection between the structure of the materials and their electrochemical performance, we first conducted the phase analysis, micromorphology characterization, and BET test on TiO₂ mesoporous microspheres and TiO₂@Fe₂O₃ microspheres; subsequently, we tested and compared the electrochemical performance of these two materials as anode materials for lithium-ion batteries and discussed the differences in the electrochemical performance of the materials before and after coating. To further explore the synergistic effect of TiO₂ and Fe₂O₃, calculations using density functional theory were made for TiO₂, Fe₂O₃, and TiO₂@Fe₂O₃. The results indicated that the composite of TiO₂ and Fe₂O₃ changed the electron density of states of the material, which led to a significant increase in electrical conductivity. This research offers a novel strategy for identifying suitable anode materials for commercial lithium-ion batteries.

2. Materials and Methods

2.1. Materials

The raw materials consisted of urea (CH₄N₂O, Sinopharm Chemical Reagent Co., Shanghai, China, AR), anhydrous ethanol (C₂H₅OH, Sinopharm Chemical Reagent Co., Shanghai, China, AR), FeCl₃·6H₂O (Aladdin Reagent Co., Shanghai, China, ACS), Fe₂O₃ (Heng Xing Reagent Co., Tianjin, China, AR), commercial graphite (C, Tianjin Battery Co., Tianjin, China, AR) and tetrabutyl titanate (TBOT, Shanghai Macklin Biochemical Co., Shanghai, China, AR). Solutions were prepared with deionized water (Molecular Lab water ultra-purifier, Shanghai, China).

The precursor TiO₂ microspheres used in this study were homemade using a low-temperature modified Stöber method, which was previously reported by our group [32]. In this method, aqueous KCl and tetrabutyl titanate were added to ethanol and reacted at a low temperature of −10 °C for 5 h. The precursor was then collected by centrifugation,

washed three times with alcohol and once with water, and subsequently freeze-dried, resulting in amorphous TiO₂ microspheres.

2.2. Synthesis of Core-Shell Structure TiO₂@Fe₂O₃ Microspheres

Figure 1 illustrates the preparation method for TiO₂@Fe₂O₃ microspheres with the core-shell structure. The above-mentioned TiO₂ microspheres (0.3 g) were first ultrasonically dispersed in 100 mL of deionized water, followed by the addition of FeCl₃·6H₂O (0.5 g) and 0.5 g urea under magnetic stirring for 10 min. The above suspensions were further heated in an 80 °C water bath with magnetic stirring for 8 h to obtain intermediate microspheres according to the following reaction Equations (1) to (3):

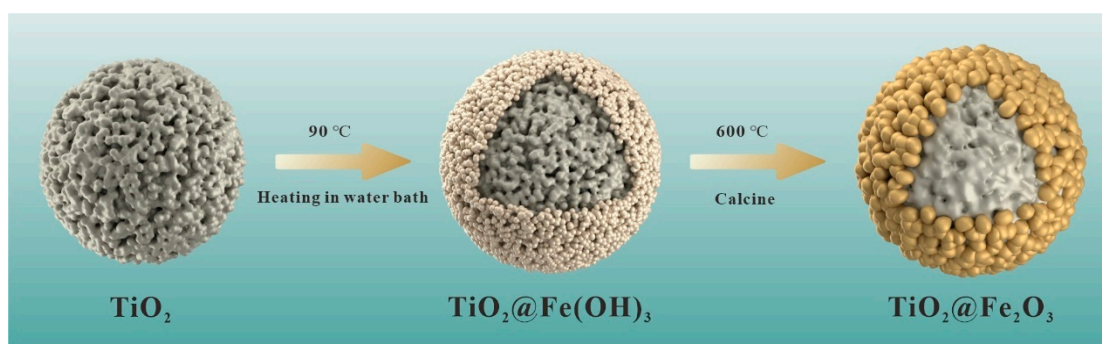
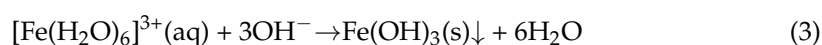
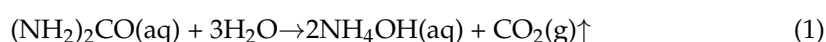


Figure 1. Preparation schematic of TiO₂@Fe₂O₃ microspheres.

The precipitate was then collected by centrifugation, washed three times with deionized water, and dried for 12 h at 50 °C. The sample was then calcined at 600 °C for 4 h. The morphology of the sample can be altered by varying the amount of FeCl₃·6H₂O added. The equation corresponding to this reaction is shown in Equation (4).



2.3. Structure Analysis and Characterization

The structural properties of the products were characterized by X-ray diffraction (XRD) using an X-ray diffractometer (PANalytical, Empyrean, Almelo, Netherlands) with Cu K α radiation ($\lambda = 0.154$ nm) and a 2θ scan range of 20–90° at a rate of 2°/min. Raman spectra were recorded on an XploRA PLUS spectrometer (HORIBA, Lille, France) using a 532 nm wavelength laser source.

The morphologies and elemental ratio of the samples were determined by a field emission scanning electron microscope (FE-SEM, SU8010, Hitachi, Tokyo, Japan) operating at 5 kV with an energy dispersive X-ray spectrometer (EDS, X-MaxN, OXFORD, Oxford, UK).

The N₂ adsorption/desorption isotherms of porous products were measured using a surface area and pore size analyzer (BET, ASAP 2020 PLUS HD88, Micromeritics, Norcross, GA, USA). The specific surface area was calculated with the Brunauer—Emmett—Teller (BET) model, and the pore size distribution was evaluated using the Barrett—Joyner—Halenda (BJH) method.

2.4. Electrochemical Tests

The anode materials, cotinine black (Shanghai Macklin Biochemical Co., Shanghai, China, AR), and the polyvinylidene fluoride (PVDF, Shanghai Macklin Biochemical Co., Shanghai, China, AR) were weighed according to the mass ratio of 8:1:1, thoroughly mixed,

and the mixed sample was then placed in a beaker with N-Methylpyrrolidone (NMP, Shanghai Aladdin Biochemical Co., Shanghai, China, AR) to be magnetically stirred for 7 h. The slurry was coated on 20 μm thick copper foil, fully dried at 80 $^{\circ}\text{C}$, and finally cut into 15 mm diameter discs. The solution of 1 M LiPF_6 was dissolved in ethylene carbonate (EC) and dimethyl carbonate (DMC) as electrolyte (EC:DMC = 1:1 vol%). Polypropylene film (Celgard 2500, Celgard Inc., Charlotte, NC, USA) was used as a separator, lithium foil was used as counter and reference electrode, and CR2032 half-cells were assembled in a glove box in an argon atmosphere. The mass loading of the electrodes was around 1.0–1.4 mg cm^{-2} . A Land CT2001A battery test system was used to measure the charge/discharge cycling performance and rate capability of the anode materials in the voltage range of 0.01–3.0 V (vs. Li/Li^+). Cyclic voltammetry (CV) analysis of the anode materials was performed using an electrochemical workstation (CS350M, Corrtest Instrument Corp., Ltd., Wuhan, China) with a voltage window of 0.01–3.5 V and a scan rate of 0.1 $\text{mV}\cdot\text{s}^{-1}$. Electrochemical impedance spectra (EIS) were tested on the same instrument in the frequency range from 1×10^6 to 0.01 Hz.

2.5. Computational Details

The density functional theory (DFT) with the pseudopotential plane-wave (PP-PW) approach, as implemented in the VASP program package [33,34], was used to compute the total energy and density of states of TiO_2 , Fe_2O_3 , and $\text{TiO}_2@Fe_2O_3$. Specifically, we employed the generalized gradient approximation (GGA) [35,36] functionals as proposed by Perdew and Wang (PW91) [37]. The cutoff energy of the plane-wave basis sets was set at 500 eV, and self-consistent electronic steps and structure relaxation were carried out until the energy and force thresholds of 1×10^{-6} eV/atom and 0.01 eV/ \AA /atom, respectively, were reached. TiO_2 and Fe_2O_3 computations were conducted using $4 \times 4 \times 4$ Monkhorst-Pack k-point meshes. By contrast, a Monkhorst-Pack k-point mesh of $4 \times 2 \times 2$ was used for $\text{TiO}_2@Fe_2O_3$ due to the large number of atoms (i.e., 299 atoms) contained in the supercell of $\text{TiO}_2@Fe_2O_3$. Every simulation run required two processes to calculate the density of states: (1) optimizing the crystal structure to obtain the lowest possible total energy, and (2) performing self-consistent simulations using the optimized structure.

3. Results and Discussion

3.1. Structural Characterization

Previously, we reported that the TiO_2 mesoporous microspheres produced in our laboratory at low temperature were amorphous [32]. Figure 2a shows the X-ray diffraction pattern of the TiO_2 mesoporous microspheres after calcination at 600 $^{\circ}\text{C}$. All the diffraction peaks in the pattern correspond to the anatase TiO_2 (ref. code: 98-009-6946) in the tetragonal crystal system, indicating that the structure of the TiO_2 mesoporous microspheres after calcination at 600 $^{\circ}\text{C}$ is the anatase phase.

Figure 2b shows the X-ray diffraction pattern of $\text{TiO}_2@Fe(OH)_3$ microspheres generated by water bath reaction prior to calcination. There are no discernible diffraction peaks in the pattern, indicating that both TiO_2 and hydroxide precipitates of Fe in $\text{TiO}_2@Fe(OH)_3$ microspheres are in an amorphous state prior to calcination. Figure 2c shows the X-ray diffraction pattern of $\text{TiO}_2@Fe(OH)_3$ microspheres after calcination at 600 $^{\circ}\text{C}$ for 4 h. The results show that all the diffraction peaks of the sample correspond to those of hematite $\alpha\text{-Fe}_2\text{O}_3$ (ref. code: 98-003-3643) in the hexagonal crystal system and anatase TiO_2 (ref. code: 98-009-6946) in the tetragonal crystal system. This indicates that the Fe(OH)_3 precipitation is transformed to $\alpha\text{-Fe}_2\text{O}_3$ through calcination, following Equation (4).

Figure 2d shows the Raman spectrum pattern of calcined $\text{TiO}_2@Fe_2O_3$ microspheres. Raman characteristic peaks of the sample at 142, 394, 525, and 634 cm^{-1} correspond to the $E_{g(1)}$, B_{1g} , A_{1g} , and $E_{g(2)}$ vibrational modes of anatase TiO_2 [38], while Raman characteristic peaks of the sample at 302 and 1318 cm^{-1} correspond to the $E_{g(1)} + E_{g(2)}$, $E_{g(3)}$ vibrational modes of hematite Fe_2O_3 [31]. No characteristic peaks corresponding to the vibrational

modes of other phases are detected, providing additional evidence that the $\text{TiO}_2@\text{Fe}_2\text{O}_3$ microspheres are composed of anatase TiO_2 and hematite Fe_2O_3 .

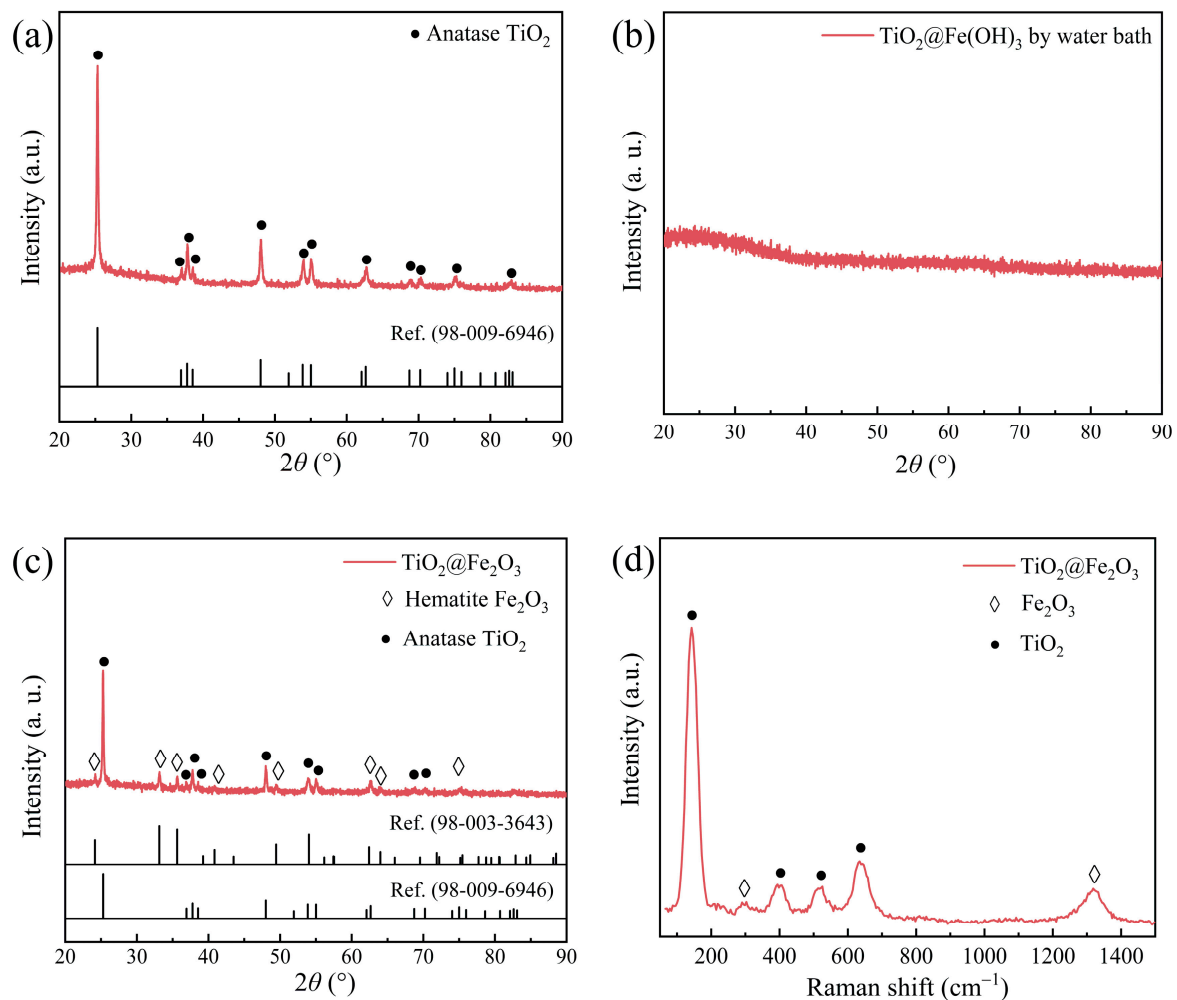


Figure 2. XRD patterns of (a) TiO_2 after 600 °C calcination, (b) $\text{TiO}_2@\text{Fe}(\text{OH})_3$ prepared by water bath, (c) $\text{TiO}_2@\text{Fe}_2\text{O}_3$ microspheres, (d) Raman spectra of $\text{TiO}_2@\text{Fe}_2\text{O}_3$ microspheres.

The above structural characterization demonstrates that after calcination, TiO_2 in $\text{TiO}_2@\text{Fe}_2\text{O}_3$ microspheres prepared by water bath reaction transforms from the early amorphous state to the anatase phase, and the hydroxide precipitation of Fe transforms to $\alpha\text{-Fe}_2\text{O}_3$ of hematite phase, with no other impurities being produced.

3.2. Morphological Characterization

Figure 3a,b display the FE-SEM images of the TiO_2 mesoporous microspheres fabricated in our laboratory by the low-temperature modified Stöber method, from which it can be observed (1) that the surface of the microspheres is rough, (2) that there is a large number of mesopores, (3) the average diameter of the microspheres is 1~2 μm , and (4) the monodispersity of the microspheres is good, which is consistent with our previous work [32]. Figure 3c,d show the FE-SEM images of the TiO_2 mesoporous microspheres after calcination at 600 °C. After calcination, the surface of the TiO_2 mesoporous microspheres becomes smooth and some mesopores are closed, which may have been caused by the decrease in the surface area of the microspheres during the phase transition of TiO_2 , hence reducing the overall surface energy of the system. The particle size of the microspheres reduced after the calcination step. This may be due to the presence of a large number of micropores inside the uncalcined microspheres. After the calcination, because of the occurrence of crystallization, some of the stomata of this microsphere be-

came closed, decreasing the microsphere volume. Figure 3e,f show the FE-SEM images of $\text{TiO}_2@\text{Fe}(\text{OH})_3$ microspheres prepared by water bath reaction, from which it can be observed that the $\text{TiO}_2@\text{Fe}(\text{OH})_3$ microspheres are uniform in size and well dispersed; compared with Figure 3a, the surface of the microspheres in Figure 3e is rougher and wrapped with a coating layer composed of fine particles, which may be the hydroxide precipitation of Fe according to the previous inference. Figure 3g,h reveal the FE-SEM images of the calcined $\text{TiO}_2@\text{Fe}_2\text{O}_3$ microspheres. Compared with Figure 3e, the particles covered on the surface of the microsphere sample in Figure 3g are larger, and these particles are interconnected and interlaced with one another. The surface of the sample is lychee-like, and it is inferred from the results in Figure 2d that the particulate matter covered on the surface should be $\alpha\text{-Fe}_2\text{O}_3$; Figure 3h shows that the monodispersity of the microspheres remains good after the calcination. The above microscopic morphological characterization indicates that after the calcination, some of the micropores on the surface of TiO_2 microspheres inside the sample are closed, and the surface coating layer is transformed from fine hydroxide precipitation of Fe to larger Fe_2O_3 particles.

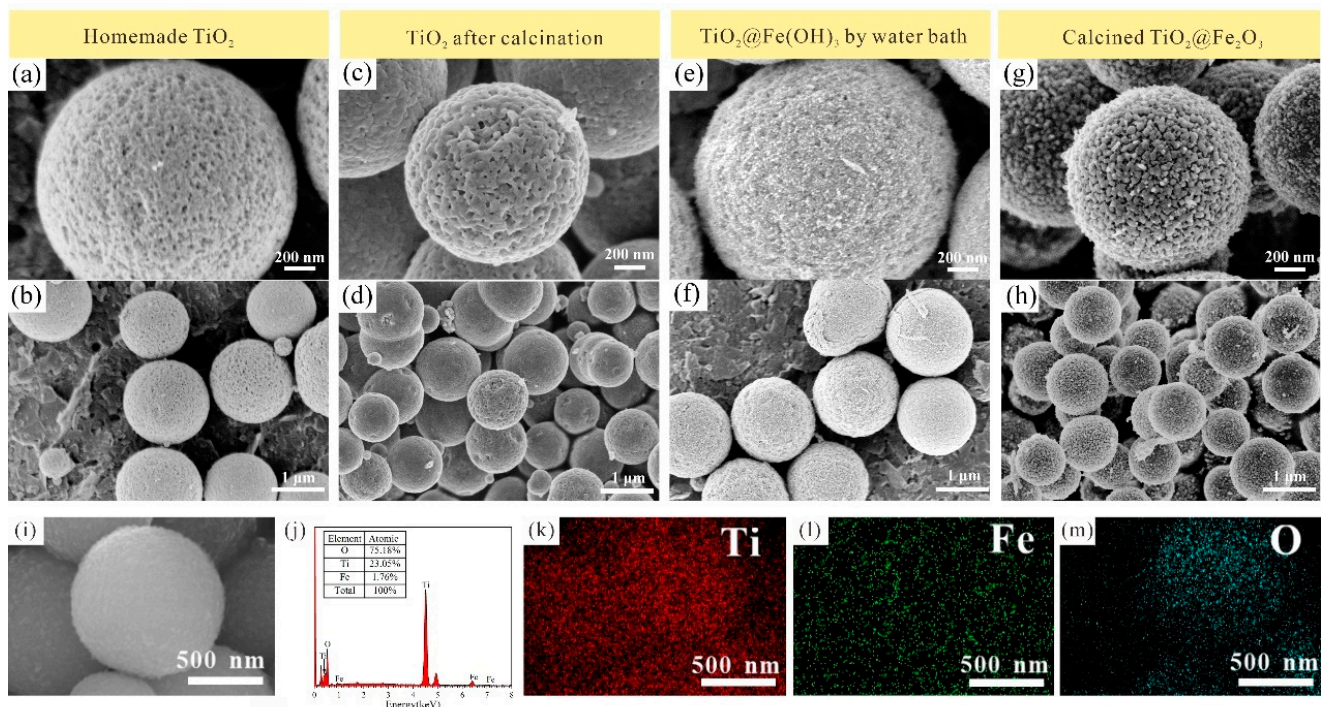


Figure 3. FE-SEM images of the (a,b) homemade TiO_2 , (c,d) TiO_2 after calcination at $600\text{ }^\circ\text{C}$, (e,f) $\text{TiO}_2@\text{Fe}(\text{OH})_3$ prepared by water bath, and (g,h) calcined $\text{TiO}_2@\text{Fe}_2\text{O}_3$ microspheres; (i,j) the EDS spectrum and (k–m) mapping images of $\text{TiO}_2@\text{Fe}_2\text{O}_3$ microspheres. The magnification of (a,c,e,g,i) is 60 k, and that of (b,d,f,h) is 20 k.

To determine the elementary composition of the calcined $\text{TiO}_2@\text{Fe}_2\text{O}_3$ microspheres, the FE-SEM image of the analysis area and the associated EDS spectrum are depicted in Figure 3i,j, respectively. It is well indicated that the $\text{TiO}_2@\text{Fe}_2\text{O}_3$ microspheres consist of Ti, Fe, and O elements, and the Ti/Fe atomic ratio is 1.75:23.05. The Fe element is significantly less than the Ti element, implying the thin thickness of the obtained Fe_2O_3 coating layer. To have a clear insight into the distribution of elements in the $\text{TiO}_2@\text{Fe}_2\text{O}_3$ microspheres, elemental mappings based on the analysis area are derived, as shown in Figure 3k–m. Perspicuously, the profiles of three-element mapping show a uniform distribution of Ti, Fe, and O elements, which further indicates a better compound between Fe_2O_3 and TiO_2 . The theoretical specific capacity C of the $\text{TiO}_2@\text{Fe}_2\text{O}_3$ microspheres is calculated from the

Fe/Ti atomic ratio, molar masses of TiO_2 and Fe_2O_3 , theoretical specific capacity of TiO_2 and Fe_2O_3 and Equation (5) and is $382.38 \text{ mAh g}^{-1}$ [39,40].

$$\begin{aligned} C(\text{TiO}_2@\text{Fe}_2\text{O}_3) &= C(\text{TiO}_2) \times \text{wt}\%(\text{TiO}_2) + C(\text{Fe}_2\text{O}_3) \times \text{wt}\%(\text{Fe}_2\text{O}_3) \\ &= 335 \times 92.95\% + 1007 \times 7.05\% = 382.38 \text{ mAh g}^{-1} \end{aligned} \quad (5)$$

3.3. BET Analysis

As shown in Figure 4a, the nitrogen adsorption—desorption isotherms of the $\text{TiO}_2@\text{Fe}_2\text{O}_3$ microspheres exhibit the type IV nitrogen adsorption branch with a type-H3 hysteresis loop, confirming the presence of mesopores in the $\text{TiO}_2@\text{Fe}_2\text{O}_3$ microspheres [7]. The Brunauer—Emmett—Teller (BET) surface area is calculated to be $14.72 \text{ m}^2/\text{g}$. Figure 4b shows the corresponding Barrett—Joyner—Halenda (BJH) pore-size distribution of the pores in the sample, and it can be seen that the pore size in the sample is mainly distributed from 1 to 10 nm, and the average pore volume is calculated to be $0.0437 \text{ cm}^3/\text{g}$. The results show that after calcination, the pores in $\text{TiO}_2@\text{Fe}_2\text{O}_3$ microspheres are mainly micropores and mesopores, which is consistent with the SEM observation.

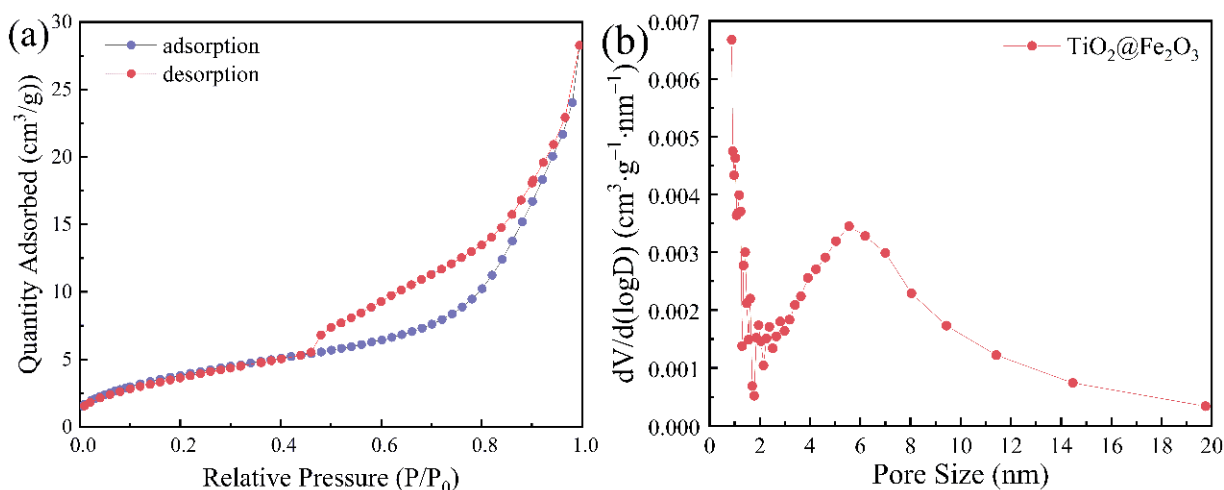
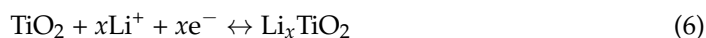


Figure 4. (a) N_2 adsorption (purple)—desorption (red) isotherms and (b) pore size distribution curves of $\text{TiO}_2@\text{Fe}_2\text{O}_3$ microspheres.

3.4. Electrochemical Performance

To investigate the influence of the Fe_2O_3 coating layer on the electrochemical performance of TiO_2 , we fabricated half-cells with the calcined TiO_2 (anatase) and $\text{TiO}_2@\text{Fe}_2\text{O}_3$ as anode materials (working electrode), tested and compared their electrochemical performance. To compare the lithiation reactions of TiO_2 , Fe_2O_3 , and $\text{TiO}_2@\text{Fe}_2\text{O}_3$ while observing whether there are other side reactions of homemade TiO_2 , we chose a large test voltage range from 0.01 to 3.5 V. Figure 5a,b show the cyclic voltammetry curves of the above two microspheres for the initial three cycles at a scan rate of 0.1 mV/s . As shown in Figure 5a, for calcined TiO_2 , a distinct reduction peak first appears at 1.7 V during the first discharge, which together with the oxidation peak at 2.2 V during the charging process corresponds to the characteristic peaks of the lithium-ion insertion/extraction reactions in anatase TiO_2 [8], as shown in Equation (6).



Subsequently, a significant reduction peak appears at 0.6 V and disappears in subsequent cycles, which may be due to the insertion of Li^+ into the irreversible site and the generation of the solid electrolyte interphase (SEI) layer [38,39]. In the two subsequent cycles, there is a tendency for the CV curves to overlap, indicating a gradual stabilization of the lithium-ion insertion/extraction reaction in the TiO_2 anode material.

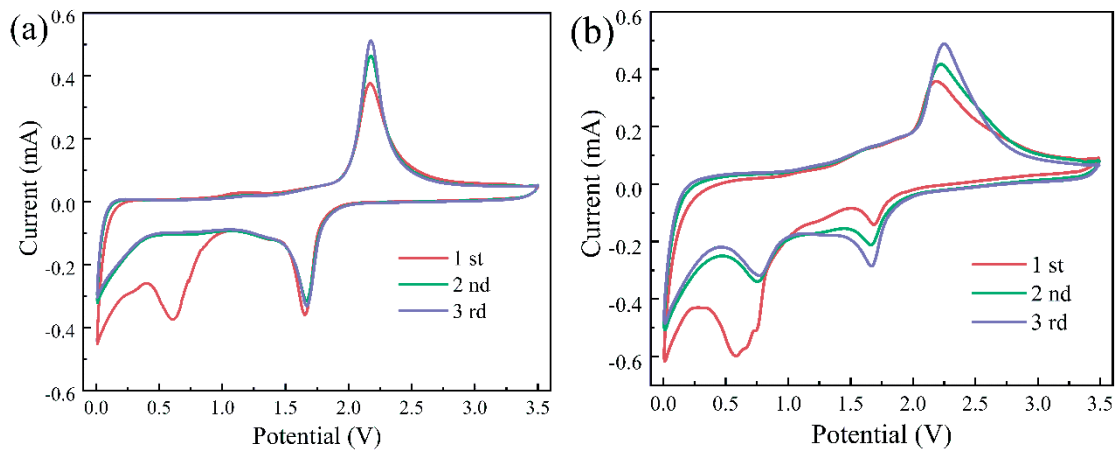
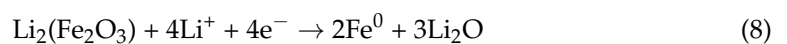
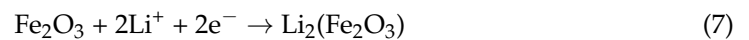


Figure 5. CV curves of (a) anatase TiO_2 and (b) $\text{TiO}_2@Fe_2O_3$ microspheres in the potential window of 0.01~3.5 V with a scanning rate of $0.1 \text{ mV}\cdot\text{s}^{-1}$.

As shown in Figure 5b, for the $\text{TiO}_2@Fe_2O_3$ microsphere anode material, the reduction peak first appears at 1.7 V during the first discharge, and this peak similarly corresponds to the characteristic peak of the Li^+ insertion/extraction reaction in anatase TiO_2 together with the oxidation peak at 2.2 V during the charging process. Subsequently, a continuous reduction peak at 0.4~1.0 V corresponds to the multistep reduction of Fe_2O_3 to Fe^0 according to Equations (7) and (8), which shifts to a reduction peak at 0.7 V during the subsequent cycles [25,30]. Presumably, the disappeared reduction peak corresponds to the insertion of Li^+ into the irreversible site and the generation of the SEI layer [31] (Figure S1 shows the CV curve of hematite Fe_2O_3 , in which these peaks also appear, further proving that these peaks belong to Fe_2O_3). This reduction peak at 0.7 V together with the broad oxidation peak at 1.5~2.0 V during the charging process corresponds to the characteristic peaks of the Li^+ insertion/extraction reactions in $\alpha\text{-Fe}_2O_3$ as shown in Equation (9).



Therefore, the total Li^+ insertion/extraction reactions of $\text{TiO}_2@Fe_2O_3$ microsphere anode material are shown in Equations (6) and (9). In the two subsequent cycles, the CV curves tend to overlap, demonstrating that the Li^+ insertion/extraction reactions in $\text{TiO}_2@Fe_2O_3$ gradually stabilize.

Figure 6a depicts the charge/discharge curves of the anode material calcined anatase TiO_2 at a current density of 0.2 C. During the first discharge, a distinct plateau appears at 1.75 V. This plateau together with the one appearing at 2.0 V during the charging process corresponds to the insertion/extraction process of lithium-ions in the interstitial octahedral sites of anatase TiO_2 , with the chemical reaction shown in Equation (6). Subsequently, a slow ramp appears between 0.9~0.7 V and disappears in the subsequent cycles, which may be due to the generation of the SEI layer and the insertion of Li^+ into the irreversible site [38,39]. This result is in accordance with the analysis of Figure 5a. In the first charge/discharge cycle, the initial discharge- and charge-specific capacities of the battery are 335.2 and 178.6 mAh g^{-1} , respectively, corresponding to the initial coulombic efficiency (ratio of charge capacity to discharge capacity) of only 53.3%; the large capacity loss may be attributed to the generation of the SEI layer and the insertion of Li^+ into the irreversible site [38,39].

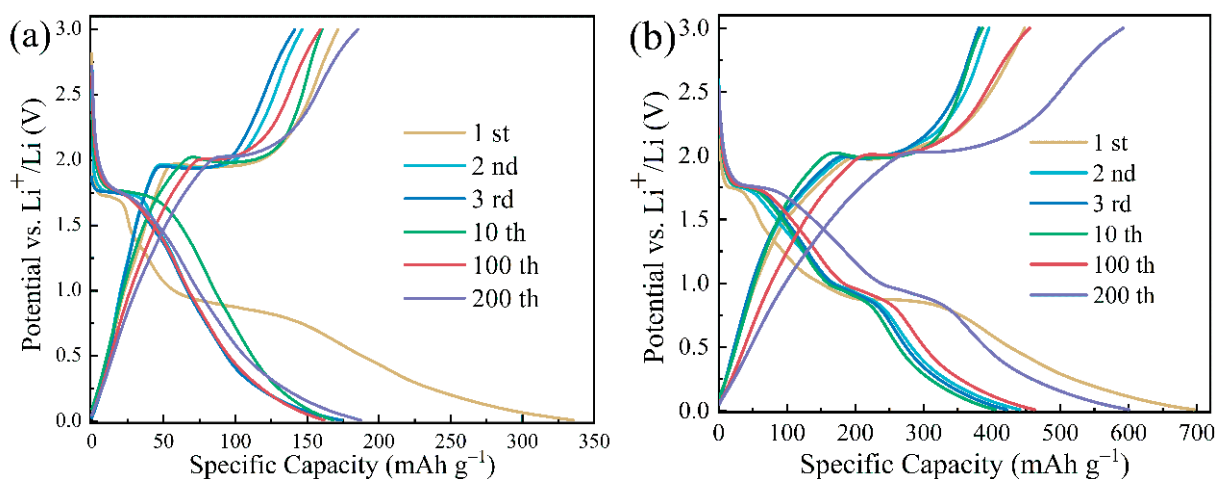


Figure 6. Galvanostatic discharge/charge curves of the 1st, 2nd, 3rd, 10th, 100th, and 200th cycles for (a) anatase TiO_2 and (b) $\text{TiO}_2@Fe_2O_3$ microspheres in the voltage range of 0.01–3.0 V at 0.2 C current density.

Figure 6b shows the charge/discharge curves of the $\text{TiO}_2@Fe_2O_3$ anode material at a current density of 0.2 C. Similarly, the plateau that appears at 1.75 V during the first discharge along with the plateau at 2.0 V during the charging process corresponds to the insertion/extraction process of lithium-ions in the interstitial octahedral sites of anatase TiO_2 . Subsequently, a distinct plateau occurs around 0.8 V, which evolves into a section of slope at 1.0–0.7 V during the following cycles. This slope, together with the slope at 1.5–2.0 V during charging, corresponds to the insertion/extraction process of lithium-ions in $\alpha\text{-Fe}_2O_3$ as shown in Equation (9), and this finding is consistent with the analysis of Figure 5b. The initial discharge- and charge-specific capacities of the $\text{TiO}_2@Fe_2O_3$ anode material are 698.5 and 476.5 mAh g^{-1} , respectively, and the reversible capacity (the portion of capacity that can participate in both charging and discharging within a single cycle, i.e., the minimum of the discharge-specific capacity and the charge-specific capacity) is 476.5 mAh g^{-1} , which is larger than the theoretical specific capacity 382.38 mAh g^{-1} of $\text{TiO}_2@Fe_2O_3$ previously obtained by calculation (see Equation (5)), which may be mainly attributed to the synergistic effect of TiO_2 and Fe_2O_3 [30,31] and the additional lithium storage sites provided by the larger specific surface area of the material (the surface of the material is more likely to form point defects, thus providing more lithium storage sites and increasing the specific capacity of the material) [40]. The initial coulombic efficiency of the material is 68.2%, and the lost capacity can still be attributed to the generation of the SEI layer and the insertion of Li^+ into the irreversible site.

After 2, 3, 10, 100, and 200 cycles, the reversible capacities of $\text{TiO}_2@Fe_2O_3$ anode material are 395.6, 381.0, 386.1, 455.2, and 591.9 mAh g^{-1} , which are much larger than those of anatase TiO_2 anode material (146.5, 141.4, 160.1, 159.1, and 185.4 mAh g^{-1}). It is interesting to note that the reversible capacity of the $\text{TiO}_2@Fe_2O_3$ material at the 200th cycle is increased by 219.3% compared with TiO_2 and is much higher than its own theoretical specific capacity of 335.2 mAh g^{-1} . According to the results of the previous EDS analysis, the mass of coated Fe_2O_3 in $\text{TiO}_2@Fe_2O_3$ microspheres only accounts for 7.05% of the total mass, and the coating of such a small amount of Fe_2O_3 brings a significant increase in the reversible capacity of the material, implying a good synergistic effect of TiO_2 and Fe_2O_3 as anode materials. The reversible capacity of both anatase TiO_2 and $\text{TiO}_2@Fe_2O_3$ microspheres is enhanced after a large number of cycles, which is a phenomenon commonly found in transition metal oxides. This may be due to the structural changes induced in the anode material when lithium-ions are continuously inserted/extracted, i.e., further activation of the material [7,40,41]. It is noteworthy that the reversible capacity of $\text{TiO}_2@Fe_2O_3$ microsphere anode material at the 200th cycle increased by 49.62% compared with the 2nd cycle, which is significantly higher than that of TiO_2 by 26.81%. The reason may be that

the $\text{TiO}_2@\text{Fe}_2\text{O}_3$ generates new interfaces after the coating of Fe_2O_3 , which reduces the activation energy of this material. With the continuous insertion/extraction of lithium-ions, the structure of the active material is more likely to change, resulting in the formation of more new effective lithium storage sites within the material during the cycling process, which leads to an increase in specific capacity. This finding is also supported by the results in Figure 7 below.

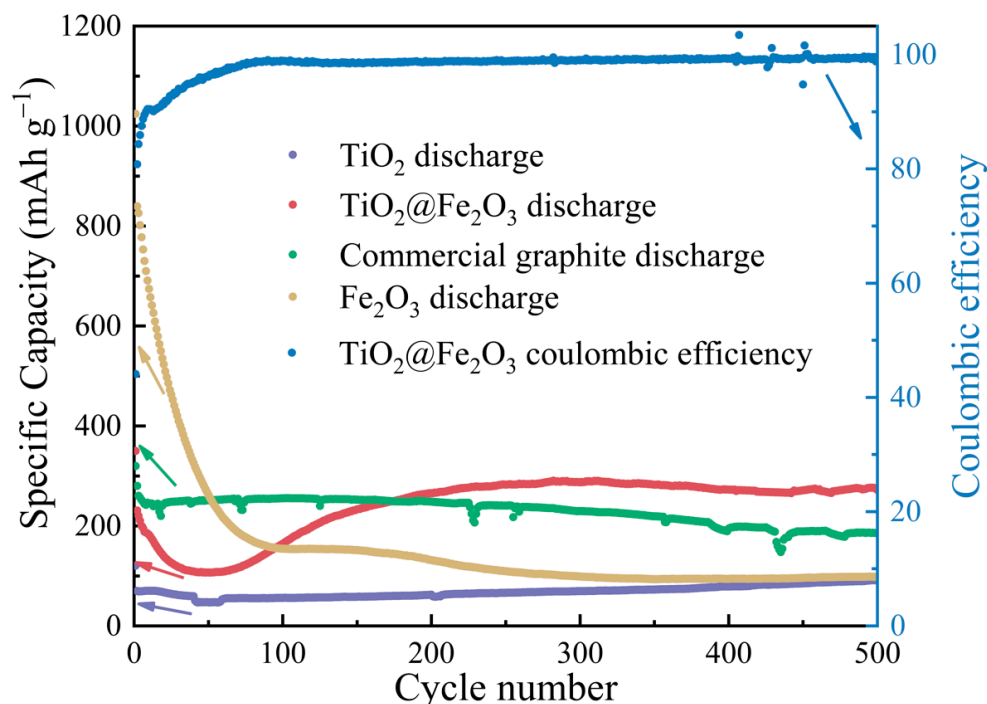


Figure 7. Cycling performances of anatase TiO_2 , $\text{TiO}_2@\text{Fe}_2\text{O}_3$, hematite Fe_2O_3 , commercial graphite and coulombic efficiency of $\text{TiO}_2@\text{Fe}_2\text{O}_3$ in the voltage range of 0.01~3.0 V at 2 C current density.

To further exhibit the cycling performance as well as the rate capabilities of the materials, we prepared half-cells with anatase TiO_2 microspheres, $\text{TiO}_2@\text{Fe}_2\text{O}_3$ microspheres, commercial graphite, and $\alpha\text{-Fe}_2\text{O}_3$ calcined at 600 °C as the anode material (working electrode), and performed cyclic charge/discharge tests at a current density of 2 C; their discharge specific capacities are shown as the purple, red, green, and brown curves in Figure 7, respectively. The discharge-specific capacities of anatase TiO_2 and $\text{TiO}_2@\text{Fe}_2\text{O}_3$ microspheres after 500 cycles are 91.6 and 273.9 mAh g^{-1} at a current density of 2 C, respectively, indicating that the $\text{TiO}_2@\text{Fe}_2\text{O}_3$ microsphere anode material with Fe_2O_3 coating exhibits a significant increase in the specific capacity after a large number of cycles, and this result is consistent with the findings demonstrated in Figure 6b. In addition, after 500 cycles, the coulombic efficiency of the $\text{TiO}_2@\text{Fe}_2\text{O}_3$ microsphere reaches 99.4%, indicating that the material has good reversibility of charge and discharge [42]. The discharge-specific capacity of the commercial graphite anode stabilizes from the 10th cycle until the 132nd cycle when it begins to decrease gradually, and the discharge-specific capacity is only 167.1 mAh g^{-1} after 500 cycles, which indicates that the $\text{TiO}_2@\text{Fe}_2\text{O}_3$ microsphere anode material has superior cycling consistency and specific capacity compared with commercial graphite. The discharge-specific capacity of the hematite Fe_2O_3 anode material has been decaying with cycling and is only 98.1 mAh g^{-1} after 500 cycles, which indicates that employing TiO_2 as the core of the $\text{TiO}_2@\text{Fe}_2\text{O}_3$ anode material can significantly improve the cycling consistency of this material (the nanoscale structure of Fe_2O_3 on the surface of the microsphere also plays an important role). The above results demonstrate that in the $\text{TiO}_2@\text{Fe}_2\text{O}_3$ microsphere anode material, TiO_2 as the inner core maintains the structural stability of the material when Li-ions are inserted/extracted, while Fe_2O_3 as the outer shell can effectively

enhance the specific capacity of the material. We are trying to explain the essential reasons for the synergistic effect of the two materials through computer simulations, which are in progress.

Figure 8 exhibits the rate performance of anatase TiO_2 microspheres, $\text{TiO}_2@Fe_2O_3$ microspheres, commercial graphite, and the calcined $\alpha\text{-Fe}_2O_3$ at $600\text{ }^\circ\text{C}$. At current densities of 100, 200, 400, 800, and 1600 mA g^{-1} , the reversible capacities of the anatase TiO_2 anode materials are 73.8, 57, 41.3, 31, and 24.7 mAh g^{-1} , respectively; the reversible capacities of the $\text{TiO}_2@Fe_2O_3$ microsphere anode materials are 394.4, 339.9, 288.2, 220.1, and 126.1 mAh g^{-1} , respectively; the reversible capacities of the commercial graphite are 317.0, 284.9, 251.9, 190.6, and 95.7 mAh g^{-1} ; and the reversible capacities of $\alpha\text{-Fe}_2O_3$ anode materials are 818.8, 378.6, 255.9, 172.5, and 125.6 mAh g^{-1} , respectively. The reversible capacities of $\text{TiO}_2@Fe_2O_3$ microsphere anode materials at different current densities are significantly larger than those of TiO_2 and commercial graphite anode materials, indicating that $\text{TiO}_2@Fe_2O_3$ microsphere anode material has the potential for the application. For the calcined $\alpha\text{-Fe}_2O_3$ anode material, the specific capacity decays at different current densities due to the absence of a solid TiO_2 core to support the structure, and this finding is consistent with the results presented in Figure 7. At the end of the test at the current density of 1600 mA g^{-1} , the four materials are then cycled at a current density of 100 mA g^{-1} . From the results shown in Figure 8, it can be found that the specific capacities of the three materials—anatase TiO_2 microspheres, $\text{TiO}_2@Fe_2O_3$ microspheres, and commercial graphite—are not significantly different from those measured at 100 mA g^{-1} at the beginning of the rate performance test, suggesting that the charge-discharge cycles at high current density do not significantly damage the structural integrity of the three materials [43]. The above results show that the rate performance of the $\text{TiO}_2@Fe_2O_3$ microsphere anode material is significantly improved after the coating of Fe_2O_3 compared with that of anatase TiO_2 , and we assume that this is because the Fe_2O_3 coating layer may improve the electronic conductivity of the material and enhance the lithium-ion diffusion rate in the material.

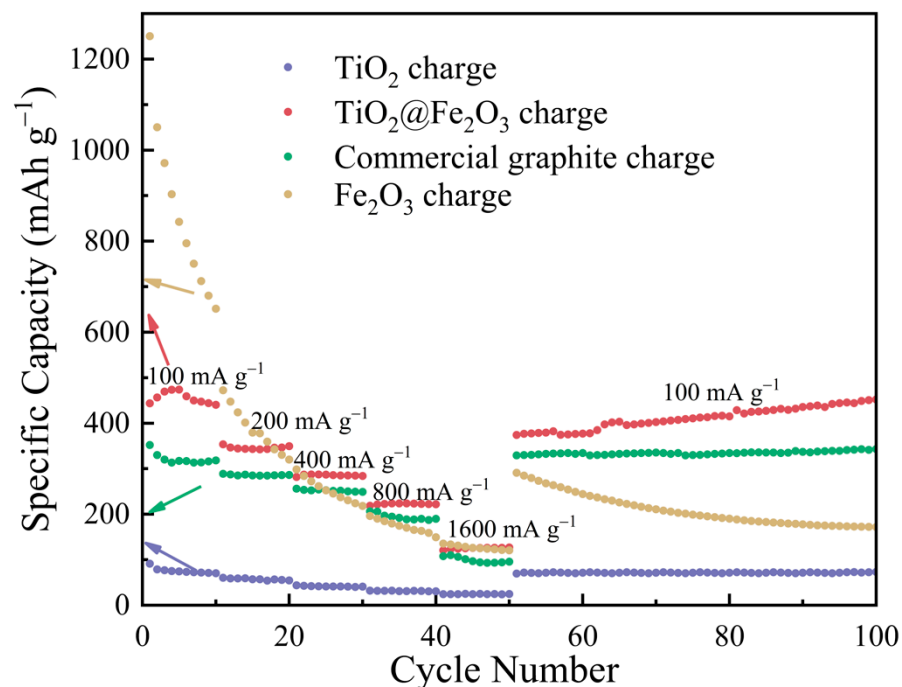


Figure 8. Rate capability tests of anatase TiO_2 , $\text{TiO}_2@Fe_2O_3$, hematite Fe_2O_3 , and commercial graphite at rates of 100, 200, 400, 800, 1600, and 100 mA g^{-1} in sequence.

To further investigate the influence of the Fe_2O_3 coating layer on the electronic conductivity of the anode materials, we conducted EIS tests on anatase TiO_2 , $\text{TiO}_2@Fe_2O_3$ microsphere, and hematite Fe_2O_3 , respectively, and the results are shown in Figure 9.

The Nyquist plots of all three materials consist of a semicircle in the high- and medium-frequency region and a slant line in the low-frequency region. The half circle in the high- and medium-frequency region reflects the impedance of the material, which includes the internal resistance of the cell and the charge transfer impedance, the smaller the radius of the half circle, the smaller the impedance; the slope of the slant line in the low-frequency region reflects the lithium-ion diffusion rate in the anode material, and the greater the slope of the slant line, the faster the diffusion rate of Li-ions [44]. Based on the lithium-ion insertion/extraction mechanism in the anode material, the EIS profile can be fitted based on an equivalent circuit (inset in Figure 9). R1 is the ohmic resistance (total resistance of the electrolyte, separator, and electrical contacts), R2 is the charge transfer resistance, Wo1 is the Warburg impedance of lithium-ion diffusion into the active materials, and CPE1 is the constant phase-angle element, which involves double layer capacitance [45]. The fitted results are shown in Table 1. The charge transfer impedances of anatase TiO₂ microspheres, TiO₂@Fe₂O₃ microspheres, and α -Fe₂O₃ anode materials are 238.35, 119.81, and 202.17 Ω , respectively, and these impedances reflect the conductivity of the three materials, among which, the conductivity of TiO₂@Fe₂O₃ microsphere anode material is significantly higher than that of the other two materials and the results of DFT simulations later in the paper also confirm this finding. For the low-frequency region, the slope of the slant line of TiO₂@Fe₂O₃ microsphere anode material is significantly larger than that of TiO₂ as well as Fe₂O₃, and the slope of the slant line of Fe₂O₃ is larger than that of TiO₂. This indicates that the lithium-ion diffusion rate is the highest in TiO₂@Fe₂O₃ microsphere anode material, which is mainly attributed to the higher lithium-ion diffusion rate of Fe₂O₃ (1×10^{-14} to 1×10^{-11} cm² s⁻¹) [46] relative to TiO₂ (1×10^{-15} to 1×10^{-9} cm² s⁻¹) [7] and the unique porous and core-shell structure of TiO₂@Fe₂O₃ microspheres that shorten the diffusion distance of lithium-ions. The above results reveal that the electronic conductivity of TiO₂@Fe₂O₃ microsphere anode material and the diffusion rate of lithium-ions inside it are significantly improved relative to anatase TiO₂. It has been reported in the literature [25,47] that the increase in the electronic conductivity of the material and the diffusion rate of lithium-ions inside it can enhance the rate properties of the material, which is consistent with the results demonstrated in Figure 8.

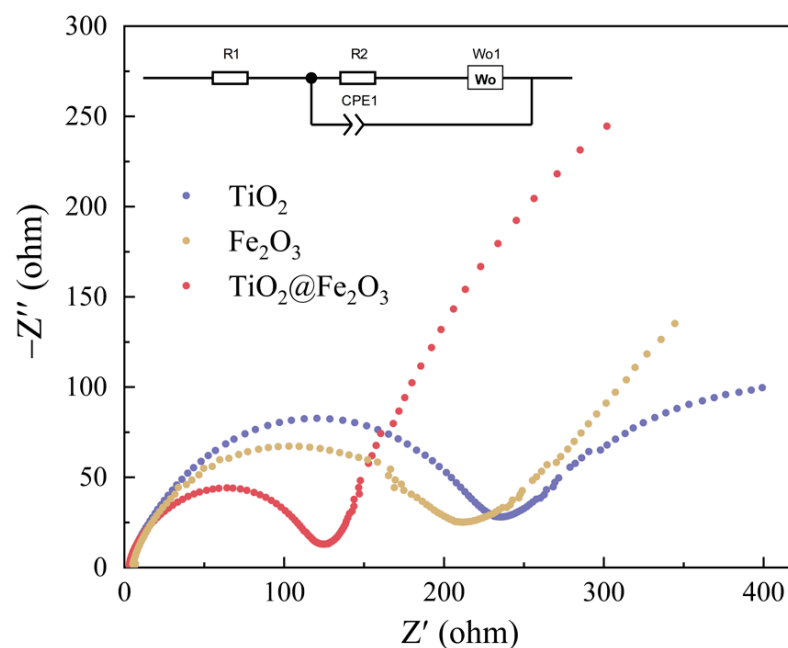


Figure 9. Nyquist plots of anatase TiO₂, TiO₂@Fe₂O₃, and hematite Fe₂O₃ in the frequency range from 0.01 to 1×10^6 Hz. The inset is the corresponding equivalent circuit.

Table 1. R1 (ohmic resistance) and R2 (charge transfer impedance) values obtained from equivalent circuit fitting for anatase TiO₂, TiO₂@Fe₂O₃ microspheres, and hematite Fe₂O₃ materials in LIBs.

Materials	R1	R2
TiO ₂	2.29	238.35
TiO ₂ @Fe ₂ O ₃	2.08	119.81
Fe ₂ O ₃	4.03	202.17

3.5. First-Principles Calculations

Figure 9 demonstrates that the electronic conductivity of TiO₂@Fe₂O₃ microsphere anode material is significantly greater than that of TiO₂ and Fe₂O₃. To explain this finding and investigate further the synergistic effect of TiO₂ and Fe₂O₃, we used density functional theory to calculate the electron density of states (DOS) of anatase TiO₂, hematite Fe₂O₃, and TiO₂@Fe₂O₃. Figure 10a depicts the crystal structure of anatase TiO₂, which belongs to the tetragonal system and has structurally optimized lattice constants of $a = b = 3.803 \text{ \AA}$ and $c = 9.748 \text{ \AA}$. Figure 10d illustrates the DOS map of anatase TiO₂ with a forbidden bandwidth of 2.14 eV near the Fermi level, indicating that anatase TiO₂ is a semiconductor with poor conductivity. As shown in Figure 10b, the crystal structure of hematite Fe₂O₃ is derived from its XRD test results, which belongs to the hexagonal system with $a = b = 5.035 \text{ \AA}$, $c = 13.763 \text{ \AA}$, $\alpha = \beta = 90^\circ$, $\gamma = 120^\circ$. There is a band gap around 0.4 eV for the majority spin, and no band gap for the minority spin, suggesting the hematite Fe₂O₃ is a half-metal with slightly higher electrical conductivity than anatase TiO₂. The high-energy crystal plane of TiO₂ is the (101) plane, while the high-energy crystal plane of Fe₂O₃ is the (104) plane [48]. Therefore, we constructed the interface model of TiO₂@Fe₂O₃ using the (101) plane of TiO₂ and the (104) plane of Fe₂O₃, and the total number of atoms is 299, as depicted in Figure 10c. Figure 10f is the DOS map of TiO₂@Fe₂O₃, whose spin-up and spin-down show metallicity near the Fermi level, indicating that TiO₂@Fe₂O₃ is a good conductor, and its electronic conductivity is significantly higher than that of anatase TiO₂ and hematite Fe₂O₃. This may be due to the formation of complex chemical bonds at the interface of TiO₂ and Fe₂O₃, where some Ti atoms enter the lattice of Fe₂O₃, causing a change in the electron cloud state at the interface. The high electronic conductivity gives an enhancement to the rate performance of TiO₂@Fe₂O₃ microsphere anode material, which is consistent with the experimental results in Figure 8.

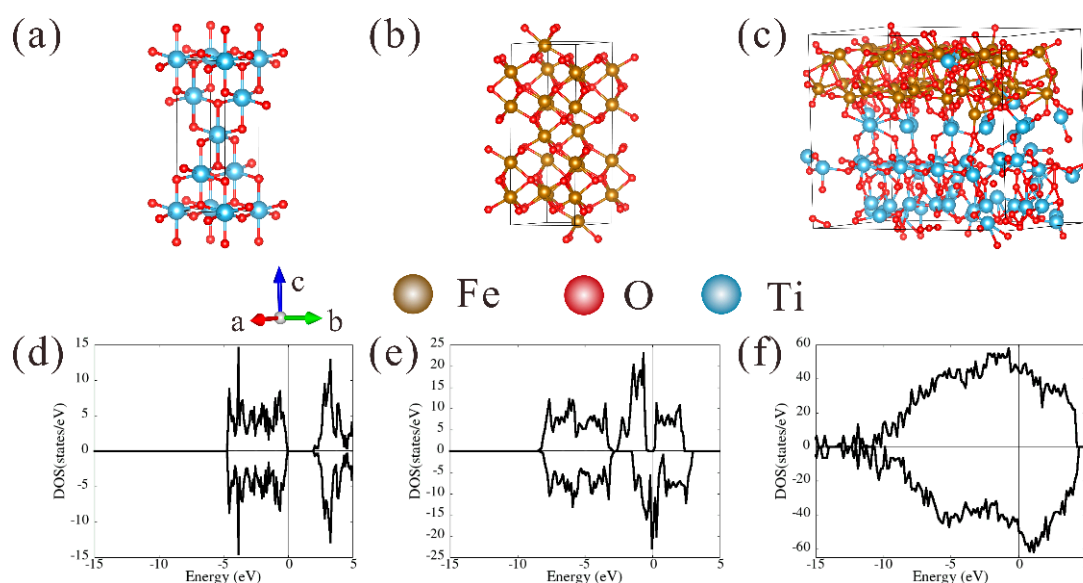


Figure 10. Optimized structures of (a) anatase TiO₂, (b) hematite Fe₂O₃, and (c) TiO₂@Fe₂O₃; corresponding electron density of states (DOS) of (d) anatase TiO₂, (e) hematite Fe₂O₃, and (f) TiO₂@Fe₂O₃.

4. Conclusions

In this study, TiO₂@Fe₂O₃ microsphere anode material is prepared by the homogeneous precipitation method. The results of XRD and Raman spectroscopy indicate that the material consists of anatase TiO₂ and hematite Fe₂O₃ (α -Fe₂O₃). SEM and EDS characterization showed that α -Fe₂O₃ is uniformly coated on the TiO₂ surface, and the surface of TiO₂@Fe₂O₃ microspheres is lychee-like, in addition, the monodispersity of the microspheres is good, and the α -Fe₂O₃ coating layer accounts for about 7.05% of the total mass. The BET results show that the TiO₂@Fe₂O₃ anode material has a large number of mesopores and micropores on the surface with a specific surface area of 14.72 m²/g.

The small amount of Fe₂O₃ coating brings a substantial improvement to the electrochemical performance of TiO₂@Fe₂O₃ microsphere anode material. After 200 cycles at a current density of 0.2 C, the specific capacity of TiO₂@Fe₂O₃ anode material increases by 219.3% compared with anatase TiO₂, reaching 591.5 mAh g⁻¹. After 500 cycles at 2 C current density, the discharge-specific capacity of TiO₂@Fe₂O₃ reaches 273.1 mAh g⁻¹, which is higher than that of commercial graphite 167.9 mAh g⁻¹ under the same test conditions. In addition, TiO₂@Fe₂O₃ microsphere anode material outperforms commercial graphite in terms of cycling consistency as well as rate performance. The EIS results demonstrate that the electronic conductivity of the TiO₂@Fe₂O₃ microsphere anode material is higher than that of anatase TiO₂ and hematite Fe₂O₃, which is the primary reason for its improved rate performance, and it also suggests a synergistic effect between TiO₂ and Fe₂O₃. From DFT calculations, the DOS of TiO₂@Fe₂O₃ shows a metallic nature, revealing the essential reason for the high electronic conductivity of TiO₂@Fe₂O₃. At present, the synergistic effect between TiO₂ and Fe₂O₃ is under further study. This study presents a novel strategy for identifying suitable anode materials for commercial lithium-ion batteries.

Supplementary Materials: The following supporting information can be downloaded at: <https://www.mdpi.com/article/10.3390/ma16051945/s1>, Figure S1: CV curves of hematite Fe₂O₃ at the scanning rate of 0.1 mV s⁻¹ in the range of 0.01~3.5 V.

Author Contributions: Conceptualization, Y.C. and F.L.; methodology, Y.C., J.W., M.-C.R. and P.B.; software, F.L., J.W., H.W. and X.Z.; validation, Y.C., M.-C.R. and P.B.; formal analysis, Y.C.; investigation, F.L., M.D. and Y.Z.; resources, Y.C.; data curation, F.L.; writing—original draft preparation, Y.C.; writing—review and editing, J.W., M.-C.R. and P.B.; visualization, F.L. and M.D.; supervision, Y.C., M.-C.R. and P.B.; project administration, Y.C., M.-C.R. and P.B.; funding acquisition, Y.C., M.-C.R. and P.B. All authors have read and agreed to the published version of the manuscript.

Funding: This research was funded by the Natural Science Foundation of Hubei Province (grant number 2020CFB408), Hubei Provincial Key Laboratory of Green Materials for Light Industry (grant number 201710A06), Hubei Province Key Research Foundation for Water Resources (grant number HBSLKY2023035) and the Open Fund of Hubei Longzhong Laboratory (grant number 2022ZZ-16).

Institutional Review Board Statement: Not applicable.

Informed Consent Statement: Not applicable.

Data Availability Statement: Data are available upon request to the corresponding author.

Conflicts of Interest: The authors declare no conflict of interest.

References

1. Ma, J.; Guo, X.; Yan, Y.; Xue, H.; Pang, H. FeO_x-based materials for electrochemical energy storage. *Adv. Sci.* **2018**, *5*, 1700986. [[CrossRef](#)] [[PubMed](#)]
2. Yu, S.; Ng, V.M.H.; Wang, F.; Xiao, Z.; Li, C.; Kong, L.B.; Que, W.; Zhou, K. Synthesis and application of iron-based nanomaterials as anodes of lithium-ion batteries and supercapacitors. *J. Mater. Chem. A* **2018**, *6*, 9332–9367. [[CrossRef](#)]
3. Balogun, M.S.; Wu, Z.; Luo, Y.; Qiu, W.; Fan, X.; Long, B.; Huang, M.; Liu, P.; Tong, Y. High power density nitridated hematite (α -Fe₂O₃) nanorods as anode for high-performance flexible lithium ion batteries. *J. Power Sources* **2016**, *308*, 7–17. [[CrossRef](#)]
4. Zuniga, L.; Gonzalez, G.; Orrostieta Chavez, R.; Myers, J.C.; Lodge, T.P.; Alcoutlabi, M. Centrifugally spun α -Fe₂O₃/TiO₂/carbon composite fibers as anode materials for lithium-ion batteries. *Appl. Sci.* **2019**, *9*, 4032. [[CrossRef](#)]

5. Han, M.; Mu, Y.; Yuan, F.; Bai, X.; Yu, J. Vapor pressure-assisted synthesis of chemically bonded TiO₂/C nanocomposites with highly mesoporous structure for lithium-ion battery anode with high capacity, ultralong cycling lifetime, and superior rate capability. *J. Power Sources* **2020**, *465*, 228206. [[CrossRef](#)]
6. Li, X.; Zhang, F.; Zhai, B.; Wang, X.; Zhao, J.; Wang, Z. Facile synthesis of porous anatase TiO₂ nanomaterials with the assistance of biomass resource for lithium ion batteries with high-rate performance. *J. Phys. Chem. Solids* **2020**, *145*, 109552. [[CrossRef](#)]
7. Guo, S.; Liu, J.; Qiu, S.; Wang, Y.; Yan, X.; Wu, N.; Wang, S.; Guo, Z. Enhancing electrochemical performances of TiO₂ porous microspheres through hybridizing with FeTiO₃ and nanocarbon. *Electrochim. Acta* **2016**, *190*, 556–565. [[CrossRef](#)]
8. Yuan, L.; Song, K.; Liu, Z.; Yu, Y.; Yang, B.; Qiao, H.; Hu, X. Fe₂O₃ nanorods decorated with ultrafine CeO₂ as binder-free cathode to improve the performance of LiO₂ batteries. *Electrochim. Acta* **2021**, *368*, 137645. [[CrossRef](#)]
9. Zhou, T.; Shen, Z.; Wu, Y.; Han, T.; Zhu, M.; Qiao, X.; Zhu, Y.; Zhang, H.; Liu, J. A yolk-shell Fe₃O₄@void@carbon nanochain as shuttle effect suppressive and volume-change accommodating sulfur host for long-life lithium-sulfur batteries. *Nanoscale* **2021**, *13*, 7744–7750. [[CrossRef](#)]
10. Huang, A.; Chen, J.; Zhou, W.; Wang, A.; Chen, M.; Tian, Q.; Xu, J. Electrodeposition of MnO₂ nanoflakes onto carbon nanotube film towards high-performance flexible quasi-solid-state Zn-MnO₂ batteries. *J. Electroanal. Chem.* **2020**, *873*, 114392. [[CrossRef](#)]
11. Zhou, Y.; Zhang, M.; Yan, X.; Han, Q.; Dong, C.; Sun, X.; You, D.; Jiang, F. Spherical-graphite/nano-Mn₂O₃ composites as advanced anode materials for lithium half/full batteries. *J. Alloy. Compd.* **2021**, *853*, 157109. [[CrossRef](#)]
12. Weng, S.C.; Brahma, S.; Huang, P.C.; Huang, Y.C.; Lee, Y.H.; Chang, C.C.; Huang, J.L. Enhanced capacity and significant rate capability of Mn₃O₄/reduced graphene oxide nanocomposite as high performance anode material in lithium-ion batteries. *Appl. Surf. Sci.* **2020**, *505*, 144629. [[CrossRef](#)]
13. Fu, W.; Liu, T.; Hou, S.; Guo, Y.; Mei, C.; Zhao, L. Engineering MnO/C microsphere for enhanced lithium storage. *J. Alloy. Compd.* **2021**, *861*, 157961. [[CrossRef](#)]
14. Li, J.; Zhang, Y.; Li, L.; Wang, Y.; Zhang, L.; Zhang, B.; Wang, F. Formation of dumbbell and sphere-like CuO as high-performance anode materials for lithium ion batteries. *Mater. Lett.* **2020**, *261*, 127058. [[CrossRef](#)]
15. Guo, R.; Huang, X.; Lin, Y.; Cao, Y. NiO/carbon aerogel microspheres with plum-pudding structure as anode materials for lithium ion batteries. *Materials* **2020**, *13*, 2363. [[CrossRef](#)] [[PubMed](#)]
16. Wu, D.; Wang, C.; Wu, H.; Wang, S.; Wang, F.; Chen, Z.; Zhao, T.; Zhang, Z.; Zhang, L.Y.; Li, C.M. Synthesis of hollow Co₃O₄ nanocrystals in situ anchored on holey graphene for high rate lithium-ion batteries. *Carbon* **2020**, *163*, 137–144. [[CrossRef](#)]
17. Qu, D.; Sun, Z.; Gan, S.; Gao, L.; Song, Z.; Kong, H.; Xu, J.; Dong, X.; Niu, L. Two-dimensional Fe₂O₃/TiO₂ Composite Nanoplates with Improved Lithium Storage Properties as Anodic Materials for Lithium-Ion Full Cells. *ChemElectroChem* **2020**, *7*, 4963–4970. [[CrossRef](#)]
18. Asahi, R.; Morikawa, T.; Irie, H.; Ohwaki, T. Nitrogen-doped titanium dioxide as visible-light-sensitive photocatalyst: Designs, developments, and prospects. *Chem. Rev.* **2014**, *114*, 9824–9852. [[CrossRef](#)]
19. Yao, M.; Wang, H.; Qian, R.; Yao, T.; Shi, J.W.; Cheng, Y. Robust hollow TiO₂ spheres for lithium/sodium ion batteries with excellent cycling stability and rate capability. *Inorg. Chem. Front.* **2021**, *8*, 5024–5033. [[CrossRef](#)]
20. Zhao, S.; Kang, D. Enhanced electrochemical performance via using interconnected TiO₂ nanofibers to inhibit the shuttle effect. *Ionics* **2021**, *27*, 2073–2077. [[CrossRef](#)]
21. Lu, X.; Luo, F.; Tian, Q.; Zhang, W.; Sui, Z.; Chen, J. Anatase TiO₂ nanowires intertwined with CNT for conductive additive-free lithium-ion battery anodes. *J. Phys. Chem. Solids* **2021**, *153*, 110037. [[CrossRef](#)]
22. Luo, J.; Xia, X.; Luo, Y.; Guan, C.; Liu, J.; Qi, X.; Ng, C.F.; Yu, T.; Zhang, H.; Fan, H.J. Rationally designed hierarchical TiO₂@Fe₂O₃ hollow nanostructures for improved lithium ion storage. *Adv. Energy Mater.* **2013**, *3*, 737–743. [[CrossRef](#)]
23. Xu, H.; Wang, W.; Yu, G.; Qin, L.; Jiang, Y.; Ren, L.; Chen, J. Nitrogen-doped carbon-coated TiO₂/TiF₃ heterostructure nanoboxes with enhanced lithium and sodium storage performance. *ACS Appl. Energy Mater.* **2020**, *3*, 4738–4745. [[CrossRef](#)]
24. Tian, Q.; Chen, Y.; Zhang, F.; Zhang, W.; Sui, Z.; Yang, L. Hierarchical carbon-riveted 2D@0D TiO₂ nanosheets@SnO₂ nanoparticles composite for a improved lithium-ion battery anode. *Appl. Surf. Sci.* **2020**, *511*, 145625. [[CrossRef](#)]
25. Fu, Y.; Wei, Q.; Wang, X.; Shu, H.; Yang, X.; Sun, S. Porous hollow α-Fe₂O₃@TiO₂ core-shell nanospheres for superior lithium/sodium storage capability. *J. Mater. Chem. A* **2015**, *3*, 13807–13818. [[CrossRef](#)]
26. Guan, S.; Fan, Q.; Shen, Z.; Zhao, Y.; Sun, Y.; Shi, Z. Heterojunction TiO₂@TiOF₂ nanosheets as superior anode materials for sodium-ion batteries. *J. Mater. Chem. A* **2021**, *9*, 5720–5729. [[CrossRef](#)]
27. Wang, H.; Guo, P.; Zhou, T.; Wu, X.; Zeng, M. Investigation of TiO₂ surface-coating modification of MgCo₂O₄ nanorods anode material. *Mater. Lett.* **2021**, *282*, 128681. [[CrossRef](#)]
28. Li, G.; Cao, S.; Fu, L.; Wan, S.; Liu, Q. A two-step hydrothermal synthesis of TiO₂/C/FeS₂ composite as high performance anode for lithium ion batteries. *Electrochim. Acta* **2021**, *386*, 138470. [[CrossRef](#)]
29. Wang, Y.; Du, Z.; Xiao, J.; Cen, W.; Yuan, S. Polypyrrole-encapsulated Fe₂O₃ nanotube arrays on a carbon cloth support: Achieving synergistic effect for enhanced supercapacitor performance. *Electrochim. Acta* **2021**, *386*, 138486. [[CrossRef](#)]
30. Yang, J.; Wu, Q.; Yang, X.; He, S.; Khan, J.; Meng, Y.; Zhu, X.; Tong, S.; Wu, M. Chestnut-like TiO₂@α-Fe₂O₃ core-shell nanostructures with abundant interfaces for efficient and ultralong life lithium-ion storage. *ACS Appl. Mater. Interfaces* **2017**, *9*, 354–361. [[CrossRef](#)]
31. Chen, Y.; Liang, J.; Tian, Q.; Zhang, W.; Sui, Z. Facile construction of clustered Fe₂O₃/TiO₂ composite for improved lithium storage performance. *Synth. Met.* **2020**, *263*, 116353. [[CrossRef](#)]

32. Chang, Y.; He, P.; Wei, Z.; Chen, Y.; Wang, H.; Wu, C.; Zhou, Z.; Huang, H.; Kowalska, E.; Dong, S. Three-dimensional monodispersed TiO₂ microsphere network formed by a sub-zero sol-gel method. *Mater. Lett.* **2020**, *268*, 127592. [[CrossRef](#)]
33. Kresse, G.; Furthmüller, J. Efficiency of ab-initio total energy calculations for metals and semiconductors using a plane-wave basis set. *Comput. Mater. Sci.* **1996**, *6*, 15–50. [[CrossRef](#)]
34. Kresse, G.; Joubert, D. From ultrasoft pseudopotentials to the projector augmented-wave method. *Phys. Rev. B* **1999**, *59*, 1758. [[CrossRef](#)]
35. Perdew, J.P.; Wang, Y. Accurate and simple density functional for the electronic exchange energy: Generalized gradient approximation. *Phys. Rev. B* **1986**, *33*, 8800–8802. [[CrossRef](#)]
36. Burke, K.; Perdew, J.P.; Wang, Y. Derivation of a Generalized Gradient Approximation: The PW91 Density Functional. In *Electronic Density Functional Theory*; Dobson, J.F., Vigale, G., Das, M.M., Eds.; Springer: Boston, MA, USA, 1998.
37. Perdew, J.P.; Wang, Y. Accurate and simple analytic representation of the electron-gas correlation energy. *Phys. Rev. B* **1992**, *45*, 13244. [[CrossRef](#)]
38. Liu, Z.; Zhang, W.; Zhou, Z.; Liu, X.; Zhang, H.; Wei, M. Hierarchical porous anatase TiO₂ microspheres with high-rate and long-term cycling stability for sodium storage in ether-based electrolyte. *ACS Appl. Energy Mater.* **2020**, *3*, 3619–3627. [[CrossRef](#)]
39. Paul, S.; Rahman, M.A.; Sharif, S.B.; Kim, J.H.; Siddiqui, S.E.T.; Hossain, M.A.M. TiO₂ as an Anode of high-performance lithium-ion batteries: A Comprehensive Review towards Practical Application. *Nanomaterials* **2022**, *12*, 2034. [[CrossRef](#)]
40. Li, Z.; Hu, X.; Shi, Z.; Lu, J.; Wang, Z. MOFs-derived metal oxides inlaid in carbon nanofibers as anode materials for high-performance lithium-ion batteries. *Appl. Surf. Sci.* **2020**, *531*, 147290. [[CrossRef](#)]
41. Hou, S.; Wang, P.; Li, Y.; Pang, F.; Liu, M.; Luo, Y.; Zhuang, L.; Zhao, L. Podocarpus-like α -Fe₂O₃/TiO₂ composite with balsam pear texture for enhanced lithium storage. *Appl. Surf. Sci.* **2019**, *476*, 959–965. [[CrossRef](#)]
42. Zhang, X.; Chen, H.; Xie, Y.; Guo, J. Ultralong life lithium-ion battery anode with superior high-rate capability and excellent cyclic stability from mesoporous Fe₂O₃@TiO₂ core-shell nanorods. *J. Mater. Chem. A* **2014**, *2*, 3912–3918. [[CrossRef](#)]
43. Gu, X.; Chen, L.; Ju, Z.; Xu, H.; Yang, J.; Qian, Y. Controlled growth of porous α -Fe₂O₃ branches on β -MnO₂ nanorods for excellent performance in lithium-ion batteries. *Adv. Funct. Mater.* **2013**, *23*, 4049–4056. [[CrossRef](#)]
44. Qin, G.; Zeng, M.; Wu, X.; Wen, J.; Li, J. Fabrication of Fe₂O₃@TiO₂ core-shell nanospheres as anode materials for lithium-ion batteries. *J. Mater. Sci. Mater. Electron.* **2018**, *29*, 12944–12950. [[CrossRef](#)]
45. Pian, C.; Peng, W.; Ren, H.; Ma, C.; Su, Y.; Ti, R.; Chen, X.; Zhu, L.; Liu, J.; Sun, X.; et al. Robust α -Fe₂O₃@TiO₂ Core-Shell Structures with Tunable Buffer Chambers for High-Performance Lithium Storage. *Front. Chem.* **2022**, *10*, 866369. [[CrossRef](#)] [[PubMed](#)]
46. Yao, J.; Yang, Y.; Li, Y.; Jiang, J.; Xiao, S.; Yang, J. Interconnected α -Fe₂O₃ nanoparticles prepared from leaching liquor of tin ore tailings as anode materials for lithium-ion batteries. *J. Alloy. Compd.* **2021**, *855*, 157288. [[CrossRef](#)]
47. Xiao, S.; Li, X.; Li, T.; Xiang, Y.; Chen, J.S. Practical strategies for enhanced performance of anode materials in Na⁺/K⁺-ion batteries. *J. Mater. Chem. A* **2021**, *9*, 7317–7335. [[CrossRef](#)]
48. Zhu, J.; Ng, K.Y.S.; Deng, D. Micro single crystals of hematite with nearly 100% exposed {104} facets: Preferred etching and lithium storage. *Cryst. Growth Des.* **2014**, *14*, 2811–2817. [[CrossRef](#)]

Disclaimer/Publisher’s Note: The statements, opinions and data contained in all publications are solely those of the individual author(s) and contributor(s) and not of MDPI and/or the editor(s). MDPI and/or the editor(s) disclaim responsibility for any injury to people or property resulting from any ideas, methods, instructions or products referred to in the content.